## Supporting Information

## SI Materials and Methods

**Protein production and purification.** AvrM-A (residues 103–343) and avrM (46-280) were expressed in *E. coli* BL21(DE3) cells or B834 cells (SeMet-labeled protein) and purified by Ni-affinity chromatography followed by TEV protease cleavage and gel filtration as described (1). AvrM-A and avrM were concentrated to 20-90 and 10 mg/ml, respectively, and stored at -80°C.

GST-AvrM-A fusion proteins in the pET41 vector were expressed in small-scale (50 ml) in *E. coli* BL21(DE3) cells using the auto-induction method (2). The cells were grown at 310 K to mid-exponential phase ($OD_{600}$ of approximately 0.6–0.8). The temperature was then reduced to 293 K and the cultures were grown for approximately 16 h before harvesting. Cells were resuspended in 2 ml pre-chilled lysis buffer (50 mM Hepes pH 8.0, 500 mM NaCl) and lysed using a digitial sonifier (Branson). Cell debris was removed by centrifugation at 15,000 *g* for 30 min at 4°C, and the supernatant was collected and mixed with 50 µl of Glutathione Sepharose resin (GE Healthcare) for 2 hours at 4°C. The resin was then harvested by centrifugation at 1000 rpm for 1 min, and washed three times with 1 ml of 50 mM Hepes pH 8.0 and 500 mM NaCl. Bound protein was eluted with 200 µl of 50 mM Hepes pH 8.0, 500 mM and 10 mM reduced glutathione. The purity of the elution fractions was analysed by SDS-PAGE and estimated to be approximately 95%.

**Crystallization, structure determination and analysis.** Diffraction-quality crystals of native AvrM-A were obtained by hanging-drop vapor diffusion in either 30% penta-erythritol ethoxylate (15/4 EO/OH), 50 mM Bis-Tris pH 5.9-6.5 and 50 mM

ammonuim sulfate, or 20-22% PEG 1500, 50 mM Bis-Tris pH 5.9-6.2 and 50 mM ammonuim sulfate, while native avrM crystals were obtained in 0.1 M MES pH 6.5 and 1.3 M sodium citrate. SeMet-labeled AvrM-A crystals were obtained by streak-seeding in 0.1 M MMT (L-malic acid, MES, Tris) buffer pH 5.8 and 25% PEG 1500. X-ray diffraction data were collected at the MX1 and MX2 beamlines of the Australian Synchrotron using the Blu-Ice software (3), and were processed and scaled using XDS (4) and Scala (5), respectively (Table S1). High resolution limits for the native avrM and AvrM-A data were selected based on a $CC_{1/2} > 0.5$ in the outer resolution shell (6). The crystals of AvrM-A, SeMet-labeled AvrM-A, and avrM diffracted to 2.9, 3.5 and 2.6 Å resolution, respectively, and the AvrM-A crystals have the symmetry of space group $C222_1$ and contain 8 monomers in the asymmetric unit, while the avrM crystals have the symmetry of space group $P2_12_12_1$ and contain 4 monomers in the asymmetric unit. AvrM-A phase information was obtained experimentally from a Se-SAD data set using *AutoSolve* within the PHENIX suite (7), while the avrM structure was solved by molecular replacement using PHASER and a partial AvrM-A model as a template. Models of AvrM-A and avrM were built manually in Coot (8), and were refined using BUSTER-TNT (9) to final Rwork/Rfree values of 21.3/24.8 for AvrM-A and 20.3/23.7 for avrM (Table S1). Structure validation was performed using MolProbity (10). The final models of AvrM-A and avrM contain residues 113-342 and 46-280, respectively. Several of the chains in AvrM-A and avrM have no electron density in the loops connecting helices $\alpha_3$ and $\alpha_4$, or $\alpha_9$ and $\alpha_{10}$, suggesting that these regions have a disordered or flexible conformation in the crystals. Chain C is partially disordered in avrM, which results in a high average B factor for the resolution range. Coordinates and structure factors of avrM and AvrM-A have been deposited in the Protein Data Bank with ID 4BJM and

4BJN, respectively. Structural analyses were performed using Coot, PyMOL (http://www.pymol.org/; DeLano Scientific LLC), DALI (11), PDBeFold (12), and PISA (13).

**Lipid-binding assay.** Serial dilutions (400, 200, 100, 50, 25, 12.5 pmol) of PI3P and PI5P were spotted onto nitrocellulose membranes. The membranes were blocked in 4% nonfat milk in PBS overnight and then incubated with 0.25 μg/ml of purified GST-fusion proteins in PBS for 4 hours at room temperature. GST was used as a negative control. The membranes were washed three times for 10 min each in PBST (PBS + 0.1% (v/v) Tween-20), and incubated with anti-GST antibody (GE Healthcare, 1:1000 dilution) for 1 hour. The blots were rinsed, and the bound proteins were detected with an anti-goat IgG-alkaline-phosphatase conjugate (Sigma, 1:2000 dilution, 1 hour incubation) using nitroblue tetrazolium (NBT)/BCIP (Sigma) as a substrate. The membranes incubated with different proteins were developed using the same NBT/BCIP incubation time in each experiment. Point mutations for the lipid-binding assay were introduced into the AvrM-A coding sequence in the pET41 *E. coli* expression vector (Novagen using Phusion DNA polymerase site-directed mutagenesis (Finnzymes)). PCR products were digested with *Dpn*I and transformed into *E. coli* (strain DH5α), and clones were fully sequenced to confirm their integrity.

**Transient *in planta* expression assays.** The AvrM-cerulean and AvrMΔ108-153-cerulean binary expression constructs have been generated previously (1). PCR-driven site-directed mutagenesis using overlapping primers on a pBluescipt construct containing AvrM-cerulean was used to generate alanine mutations within the region

required for host-cell entry (F125L126/AA, Y142/A, L134Y142/AA, E145K146/AA, D147/A, L126L134/AA and F125L126L134Y142/AAAA). AvrM-cerulean mutants were cloned as SpeI-PvuI fragments into the vector pCAMBIA3301 between the nopaline synthase (NOS) promoter and terminator sequences (1). All AvrM-cerulean fusion constructs contain an in-frame linker encoding 7 alanines between the two coding sequences. Gene splicing by PCR-driven overlap extension was used to generate AvrM and AvrMΔ108-153 with C-terminal citrine fusions and an in-frame linker encoding GGSGG between the two coding sequences. The 9 AvrM mutations that affected PIP binding (R113E, R117E, K122E, K127E, K218E, R222E, R319E, K322E and K330E) were generated as above by site-directed mutagenesis on a pBluescipt construct containing AvrM-citrine. All AvrM-citrine sequences were cloned as SpeI-PvuI fragments into the vector pCAMBIA3301 between the NOS promoter and terminator sequences.

For interaction studies with M, AvrMΔ107 and avrMΔ45-CT-Δ34 were constructed in the binary vector pEarleyGate 201 (14). Site directed mutagenesis PCR was conducted to generate 7 individual point mutations each in AvrM-A (K226Q, K232R, L241S, I248T, T259N, P280L, I310T) and avrM (Q164K, R170K, S179L, N197T, L217P, T247I, T286I). The incorporation of mutations was checked by DNA sequencing and the constructs were transformed in Agrobacterium by electroporation.

Agrobacterium cultures of strain GV3101-pMP90 containing the binary expression constructs were prepared to an $OD_{600}$ of 1.0, 0.4, 0.2 or 0.05 in 10 mM MES (pH 5.6) buffer with 10 mM $MgCl_2$ and 200 μM acetosyringone for infiltration into W38 and W38::M tobacco leaves.

**Immunoblot analysis.** Tobacco-leaf tissue was frozen in liquid nitrogen and ground in 3× Laemmli buffer with 0.2 M DTT to extract proteins. Samples were boiled for 5 min and then spun to pellet leaf debris. Proteins were separated by SDS-PAGE and transferred by electroblotting to nitrocellulose membranes. Protein blots were probed with anti-GFP (Roche) then with sheep antimouse immunoglobulin G antibody conjugated to horseradish peroxidase (Amersham). Immunoblots were visualized with SuperSignal West Pico or West Femto chemiluminescence as described by the manufacturer (Pierce).

**Confocal Microscopy.** Agrobacterium infiltrated tobacco leaves were imaged 2 days after infiltration, either directly, or after infiltration with 0.8 M mannitol for plasmolysis. Imaging was performed on a Zeiss confocal LSM 780 microscope using a 40x water immersion objective (LD C-Apochromat 40x/1.1 W Korr M27). Images were acquired using the channel mode of Zen 2011 digital imaging software (Zeiss) with 514 nm excitation and a fixed detection window of 520–600 nm for citrine emission and 650–700 nm for chlorophyll autofluorescence.

**SI Figures**

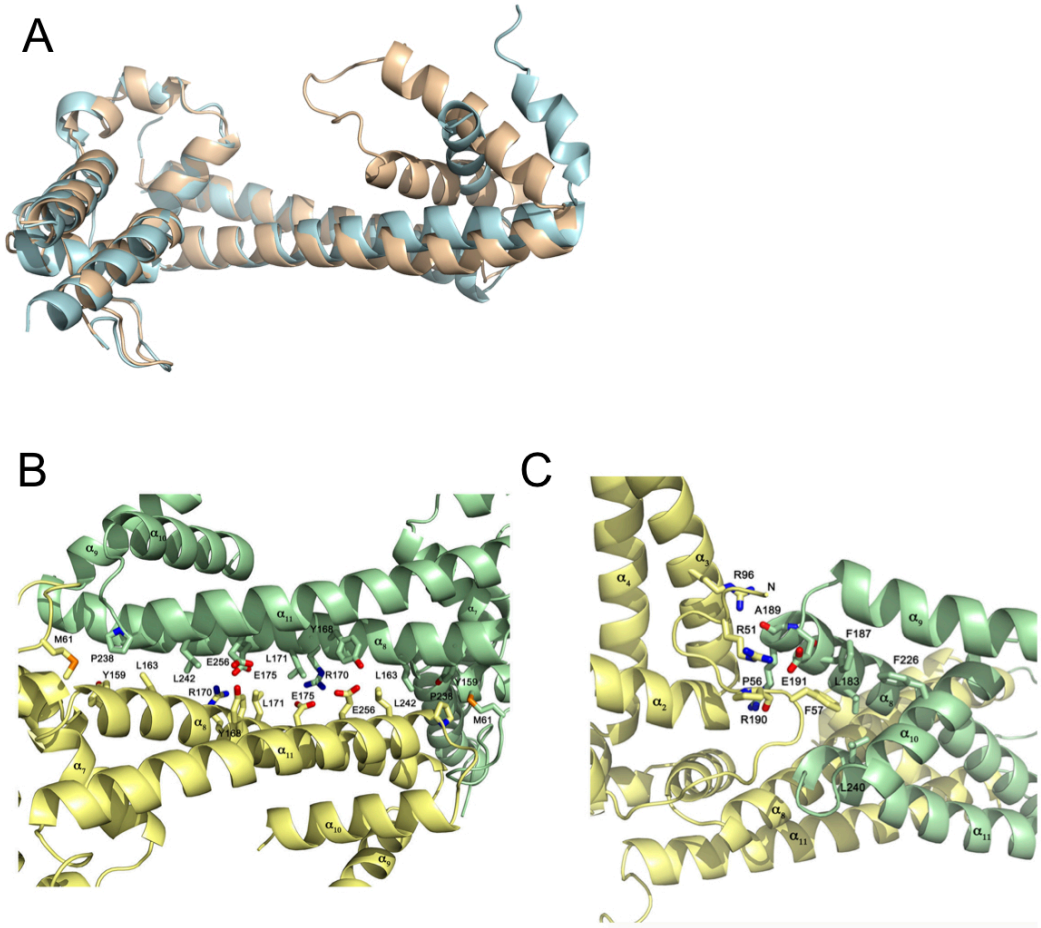


**Figure S1** Structural analysis of AvrM. (A) Superposition of the A (orange) and C (cyan) chains in AvrM-A. The G chain in AvrM-A (not shown) has a similar conformation to the C chain, and all the other chains are similar to A. (B and C) Ribbon diagrams of the avrM dimer highlighting the residues (wireframe) involved in stabilizing the dimer (as identified using the PISA server (13)). In (B) the residues stabilizing the interactions between the two C-terminal coiled-coil domains are shown, while (C) highlights the residues involved in the interaction between the N- terminal loop region of one chain, and the coiled-coil tip region of the other chain.

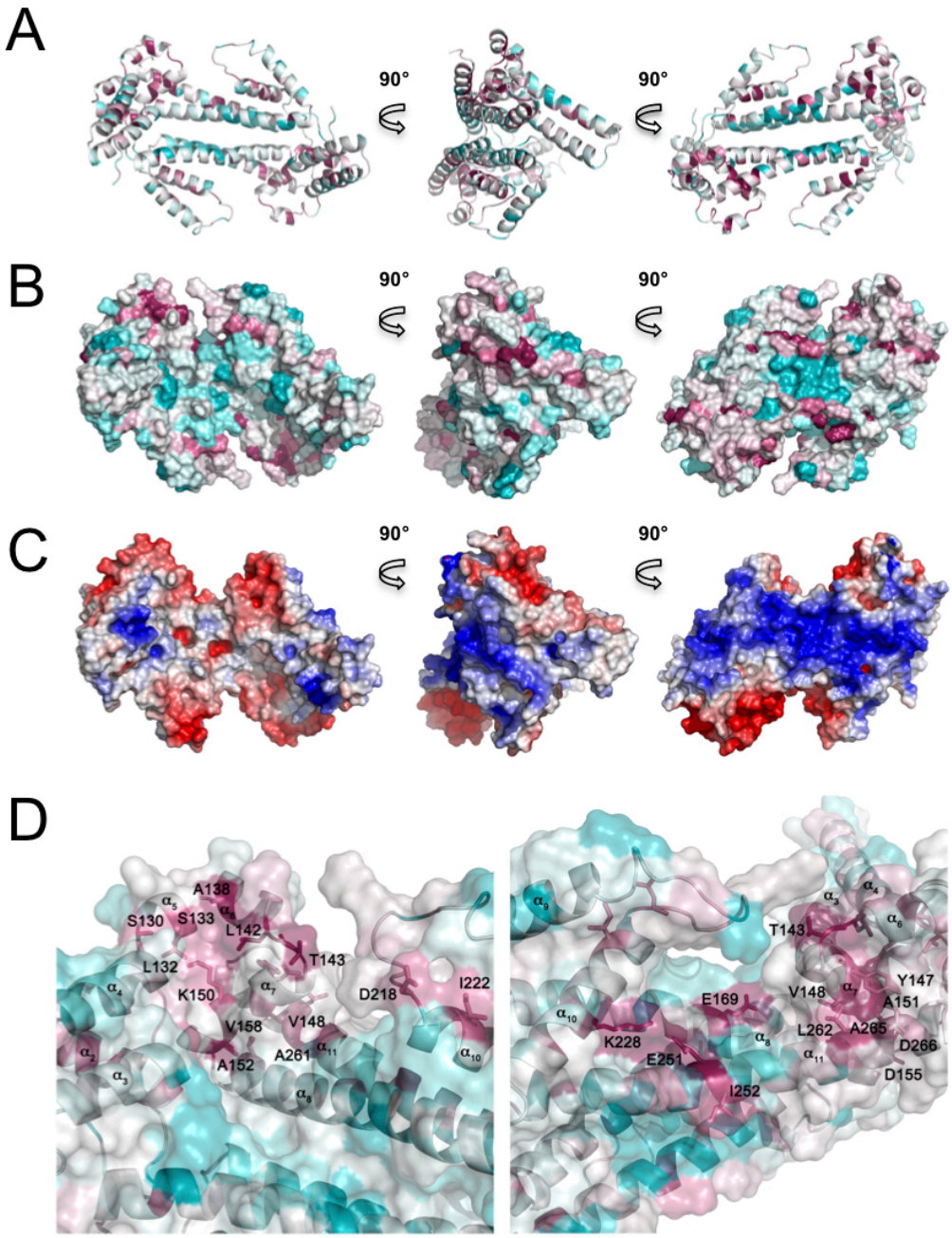


**Figure S2** Surface properties of AvrM. (A) Ribbon diagram of avrM colored by sequence conservation (as calculated using ConSurf (15)). The multiple sequence alignment used by ConSurf consisted of avrM, AvrM-A, and the Mlp homologs. The coloring is continuous from cyan (variable regions) through white to purple (conserved regions). The missing residues between the $\alpha_9$ and the $\alpha_{10}$ helices have been modeled using the AvrM-A structure as a template. (B) Surface representations

of the molecules, colored as in (A). (C) Surface representations of the molecules in (A) and (B) with electrostatic potential (calculated using APBS (16)) mapped to the surface. Coloring is continuous going from blue (potential +5 kT/e) through white to red (potential -5 kT/e). The missing residues between the $\alpha_9$ and $\alpha_{10}$ helices have not been included. (D) Transparent surface representation of the conserved surface patches in the $\alpha$-helices $\alpha_5$ to $\alpha_7$, and the anti-parallel coiled-coil region. The side-chains are displayed in wireframe, and the coloring scheme is identical to (A) and (B).

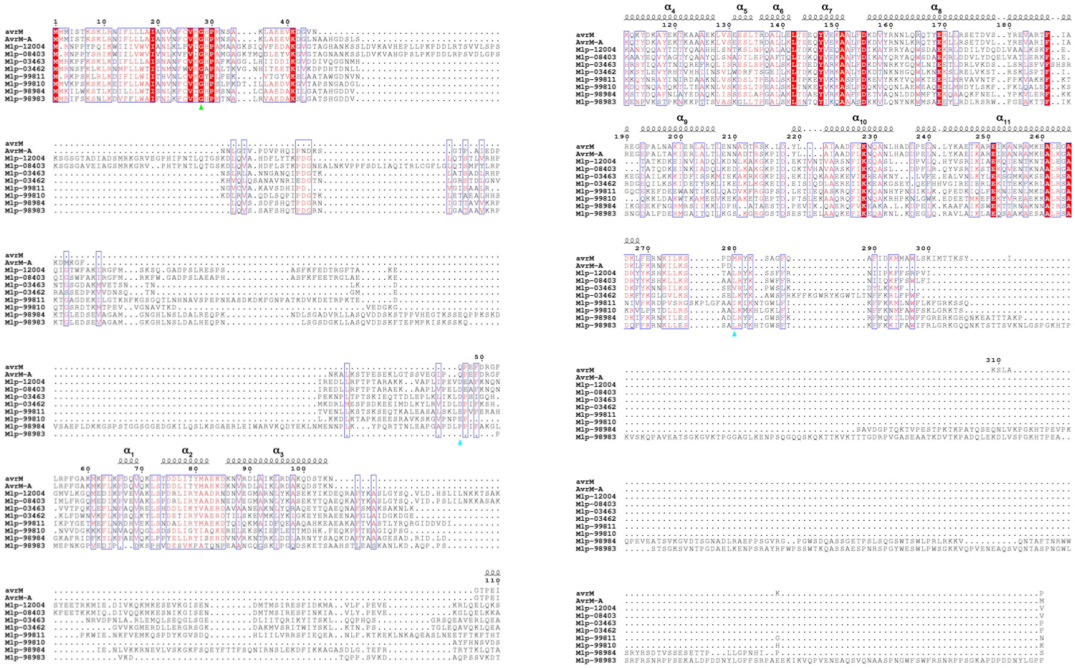

**Figure S3** Multiple sequence alignment of AvrM and the Mlp (poplar-rust/*M. larici*) homologs. Amino acid sequences of avrM, AvrM-A, Mlp-03462, Mlp-03463, Mlp-08403, Mlp-12004, Mlp-98983, Mlp- 98984, Mlp-99810 and Mlp-99811 were aligned using T-Coffee (17). The positions of the elements of secondary structure in avrM are shown at the top. The alignment was formatted using ESPript (18). Strictly conserved residues are indicated in white letters with a red box, while similar residues are indicated in red letters with a blue frame. Cyan triangles indicate the positions of the first and last residue observed in the avrM structure, while the green triangle indicates the position of the 28-aa signal sequence cleavage site.

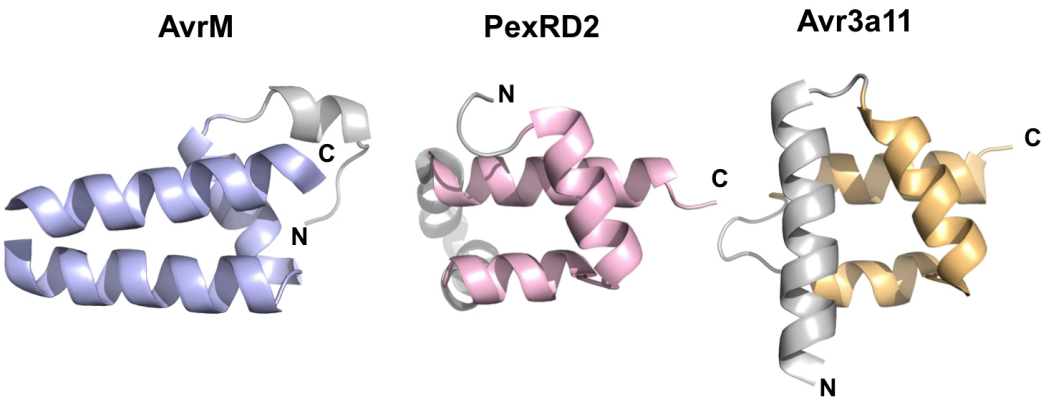


**Figure S4** Structural comparison of AvrM and the WY domain fold. The core of the WY domain in PexRD2 (pink) and Avr3a11 (orange) has a similar architecture to repeat structure identified in AvrM (blue).

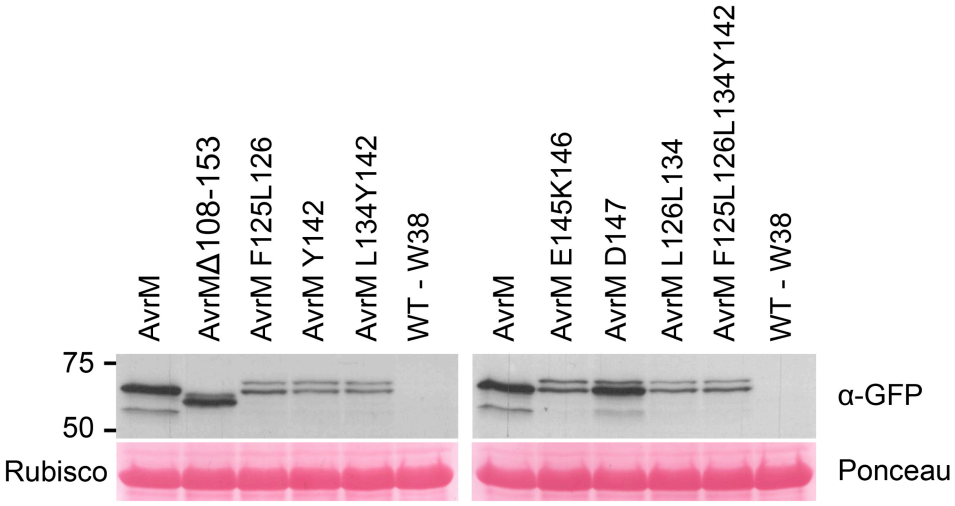


**Figure S5** Immunoblot analysis of AvrM-A. Protein extracts from tobacco-leaf tissue (WT - W38) and leaf tissue transiently expressing AvrM-A-CRL, AvrM-AΔ108-153-CRL or AvrM-A-CRL Ala mutations were analysed by immunoblotting with anti-GFP (α-GFP). Position and size (kDa) of protein molecular mass standards are indicated. Lower panel shows Ponceau S staining of protein bands on the blotted nitrocellulose membranes, showing even protein loading.

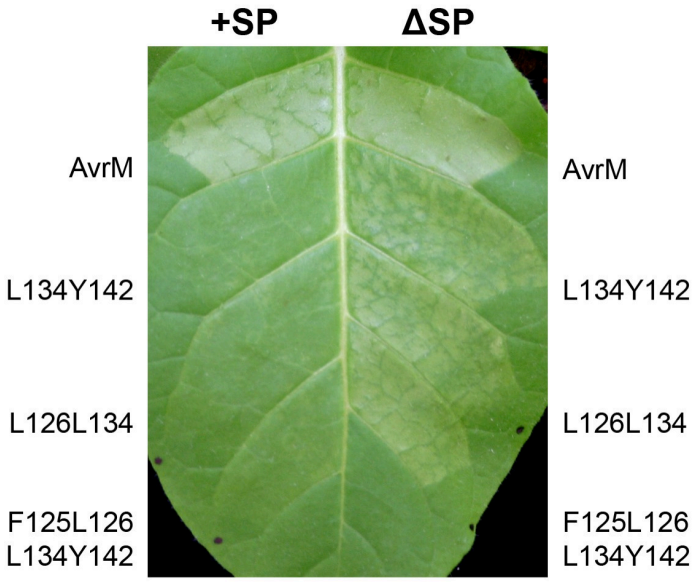


**Figure S6** Agrobacterium-mediated transient expression of AvrM-A in tobacco plants (W38). Wild-type AvrM-A (AvrM) and alanine mutants of AvrM-A (L134Y142/AA, L126L134/AA and F125L126L134Y142/AAAA) were expressed either with (+SP; left side of leaf) or without ( Δ SP; right side of leaf) the secretory signal peptide (SP). All of the AvrM constructs included a C-terminal citrine domain. Agroinfiltrations were performed at an OD600 of 0.4 and photographed 24 hours post-infiltration.

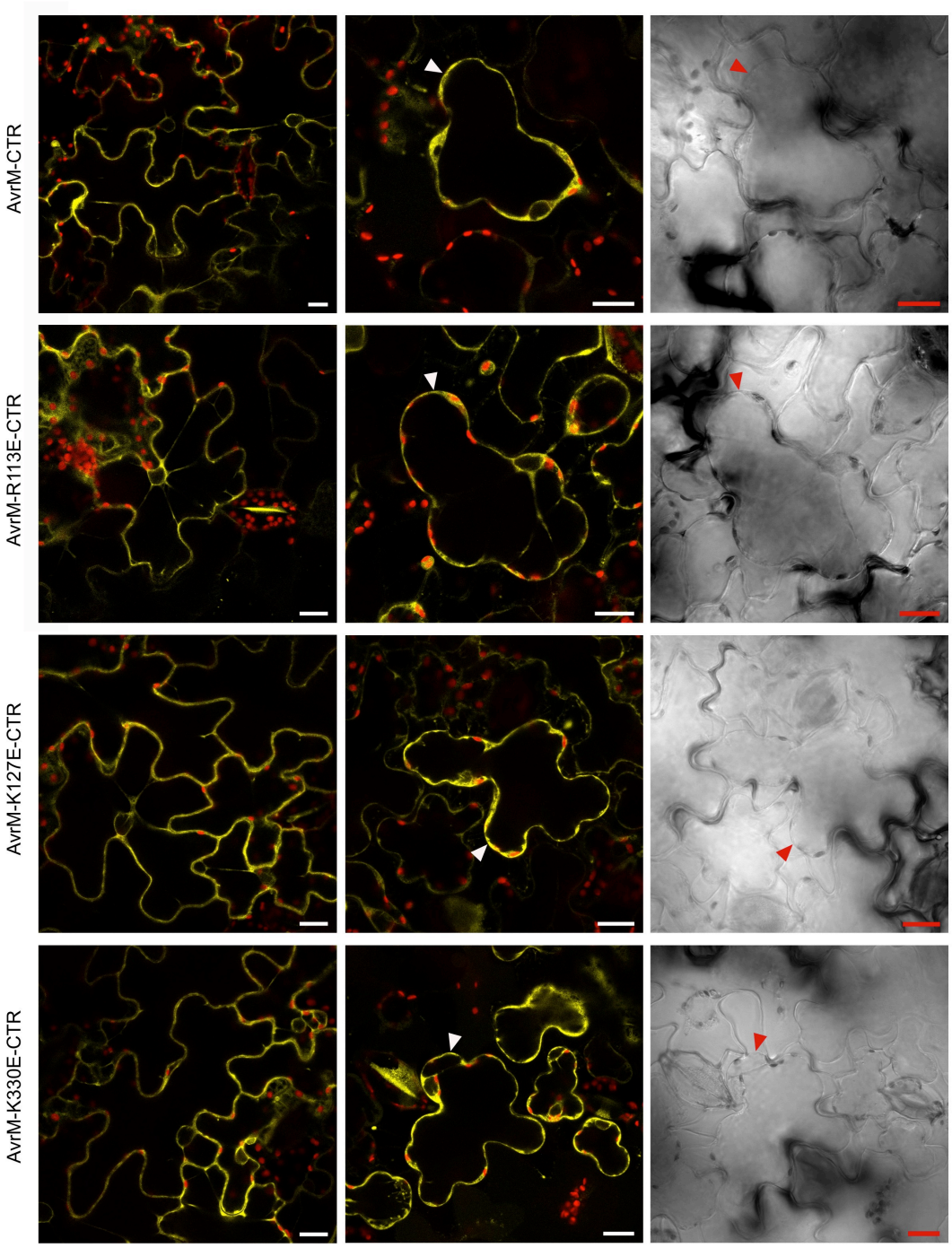


**Figure S7** Fluorescence microscopy of AvrM-A and AvrM-A PIP binding mutants transiently expressed in tobacco leaves. Confocal images of tobacco (W38) cells expressing wild-type AvrM-A or an AvrM-A PIP binding mutant (R113E, K127E, K330E), fused to citrine (CTR). The left panel shows fluorescence of untreated cells, the middle panel shows fluorescence of cells plasmolysed with 0.8 M mannitol, and the right panel shows the corresponding transmitted light images of the plasmolysed

cells. Triangles point to plasma membrane that has pulled away from the cell wall. Yellow coloration corresponds to citrine fluorescence; red coloration corresponds to chlorophyll autofluorescence. Scale bars = 20 μm.

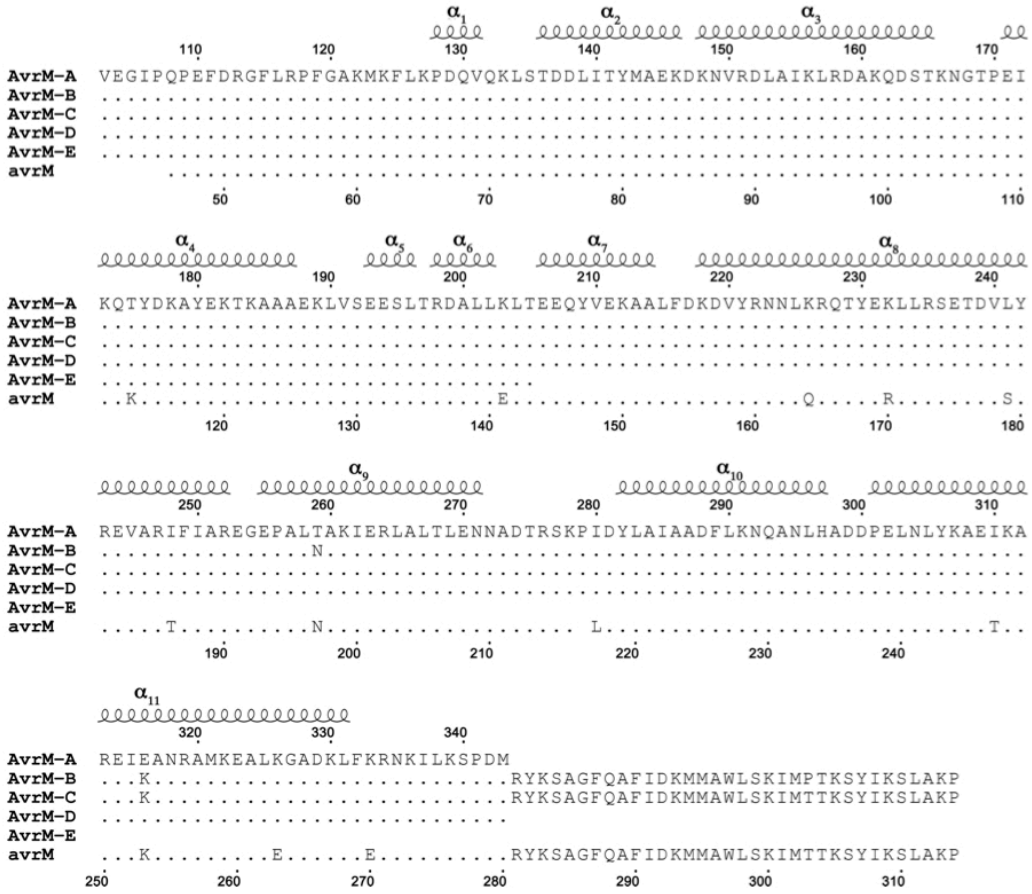


**Figure S8** Multiple sequence alignment of the different AvrM alleles. The positions of polymorphic residues are highlighted. The top and bottom sequence numbering correspond to AvrM-A and avrM, respectively.

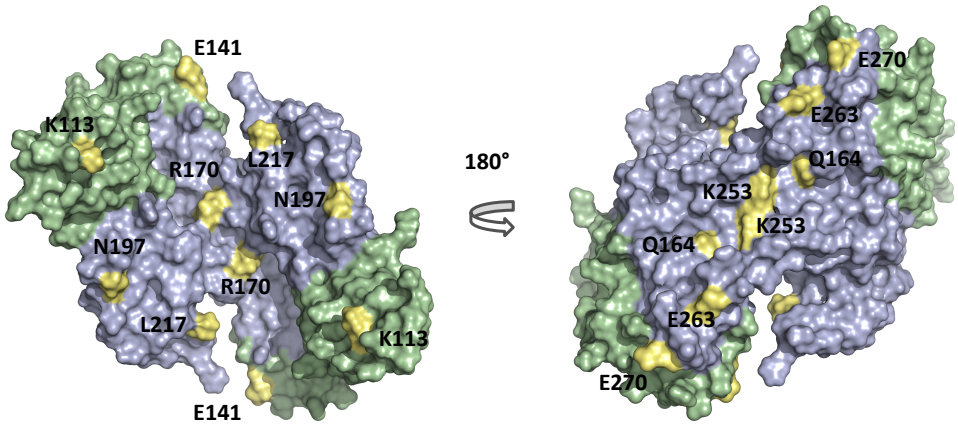


**Figure S9** Surface representations of the avrM dimer with the polymorphic residues highlighted in yellow. Deletion studies have shown that the region highlighted in blue is required for interaction with M, while the region shown in green is dispensable for M interaction.

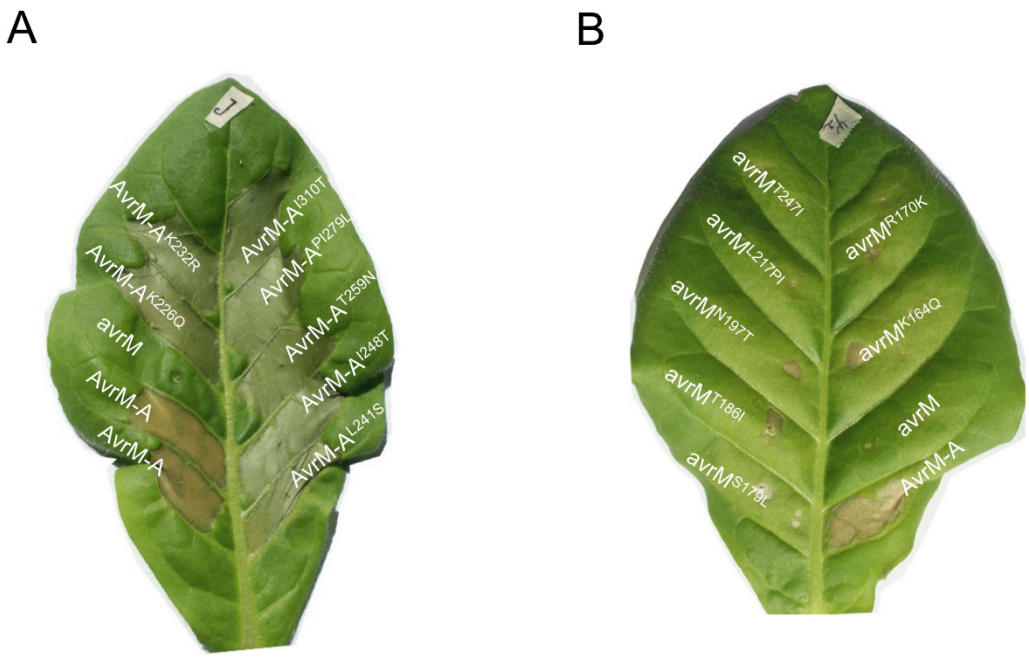


**Figure S10** Agrobacterium-mediated transient expression of AvrM-A (A) and avrM (B) mutants in leaves of transgenic tobacco plants (W38) containing the M resistance gene. Agroinfiltrations were performed at an $OD_{600}$ of 0.5, and the leaves were photographed 48 hours after infiltration.

**Table S1 Crystallographic data collection and refinement statistics.**

| | avrM | AvrM-A | SeMet AvrM-A |
|---|---|---|---|
| Diffraction data statistics | | | |
| Space group | $P2_12_12_1$ | $C222_1$ | $C222_1$ |
| Unit cell dimensions (Å) | a=88.5 | a=117.0 | a=116.4 |
| | b=125.6 | b=131.4 | b=133.7 |
| | c=128.9 | c=280.4 | c=281.5 |
| Molecules per asymmetric unit | 4 | 8 | 8 |
| Resolution range (Å) | 72.9-2.6 (2.7-2.6)[a] | 65.7-2.9 (3.0-2.9) | 93.8-3.5 (3.7-3.5) |
| No. of unique observations | 44915 | 48260 | 28160 |
| Completeness (%) | 100.0 (100.0) | 99.9 (100.0) | 100.0 (100.0) |
| Multiplicity | 7.3 (7.2) | 14.3 (14.7) | 14.9 (15.0) |
| $R_{meas}$(%)[b] | 10.5 (158) | 21.5 (273) | 21.0 (79.0) |
| $R_{p.i.m}$(%)[c] | 3.4 (59.2) | 5.6 (70.0) | 5.4 (20.4) |
| Average I/σ(I) (%) | 13.5 (1.5) | 11.3 (1.6) | 13.1 (4.4) |
| Phasing statistics (AutoSol) | | | |
| No of sites (found/all) | | | 24/32 |
| HySS CC[d] | | | 0.33 |
| SKEW[e] | | | 0.09 |
| Figure of merit[f] | | | 0.29 |
| Estimated map CC[g] | | | 0.28 +/- 0.34 |
| R factor after DM | | | 0.29 |
| Figure of merit after DM | | | 0.75 |
| Refinement statistics | | | |
| Resolution (Å) | 26.1-2.6 | 49.6-2.9 | |
| No. of reflections work set | 42535 | 45752 | |
| No. of reflections test set | 2259 | 2438 | |
| $R_{work}$ [h] (%) | 20.9 | 20.7 | |
| $R_{free}$ [i] (%) | 23.3 | 24.9 | |
| No. of protein atoms | 7092 | 13996 | |
| No. of water molecules | 126 | 0 | |
| Overall B factor ($Å^2$) | 98.2 | 96.3 | |
| R.m.s deviations from ideal values | | | |
| Bonds (Å) | 0.010 | 0.009 | |
| Angles (°) | 1.01 | 0.98 | |
| Ramachadran plot (%) | | | |
| Favoured | 99.2 | 98.1 | |
| Outliers | 0 | 0 | |

[a] Numbers in parenthesis are for the highest resolution shell.

[b] $R_{meas} = \sum_{hkl}(n_{hkl}/(n_{hkl}-1)^{1/2}\sum_i(|I_{hkl,i}-\langle I_{hkl}\rangle|))/\sum_{hkl,i}\langle I_{hkl}\rangle$, where $I_{hkl,i}$ is the intensity of an individual measurement of the reflection with Miller indices h, k and l, and $\langle I_{hkl}\rangle$ is the mean intensity of that reflection.

[c] $R_{p.i.m} = \sum_{hkl}(1/(n_{hkl}-1)\sum_i(|I_{hkl,i}-\langle I_{hkl}\rangle|))/\sum_{hkl,i}\langle I_{hkl}\rangle$.

[d] Hybrid Substructure Search, Correlation coefficient.

[e] Skew of the electron density in the map.

[f] An estimate of phase quality, ranging from 0 to 1.

[g] Bayesian correlation coefficient score. Bayesian estimates of the quality of experimental electron density maps are obtained using data from a set of previously solved datasets.

[h] $R_{work} = \sum_{hkl}(||Fobs_{hkl}|-|Fcalc_{hkl}||)/|Fobs_{hkl}|$, where $|Fobs_{hkl}|$ and $|Fcalc_{hkl}|$ are the observed and calculated structure factor amplitudes.

[i] $R_{free}$ is equivalent to $R_{work}$ but calculated with reflections (5 %) omitted from the refinement process.

**SI References**


1. Ve T, et al. (2011) Crystallization and X-ray diffraction analysis of the C-terminal domain of the flax rust effector protein AvrM. *Acta Crystallogr Sect F Struct Biol Cryst Commun* 67:1603-1607.
2. Studier FW (2005) Protein production by auto-induction in high density shaking cultures. *Protein Expr Purif* 41:207-234.
3. McPhillips TM, et al. (2002) Blu-Ice and the Distributed Control System: software for data acquisition and instrument control at macromolecular crystallography beamlines. *J Synchrotron Radiat* 9:401-406.
4. Kabsch W (2010) Xds. *Acta Crystallogr D Biol Crystallogr* 66:125-132.
5. Winn MD (2003) An overview of the CCP4 project in protein crystallography: an example of a collaborative project. *J Synchrotron Radiat* 10:23-25.
6. Karplus PA, Diederichs K (2012) Linking crystallographic model and data quality. *Science* 336:1030-1033.
7. Adams PD, et al. (2010) PHENIX: a comprehensive Python-based system for macromolecular structure solution. *Acta Crystallogr D Biol Crystallogr* 66:213-221.
8. Emsley P, Cowtan K (2004) Coot: model-building tools for molecular graphics. *Acta Crystallogr D Biol Crystallogr* 60:2126-2132.
9. Blanc E, et al. (2004) Refinement of severely incomplete structures with maximum likelihood in BUSTER-TNT. *Acta Crystallogr D Biol Crystallogr* 60:2210-2221.
10. Chen VB, et al. (2010) MolProbity: all-atom structure validation for macromolecular crystallography. *Acta Crystallogr D Biol Crystallogr* 66:12-21.
11. Holm L, Rosenstrom P (2010) Dali server: conservation mapping in 3D. *Nucleic Acids Res* 38:W545-549.
12. Krissinel E, Henrick K (2004) Secondary-structure matching (SSM), a new tool for fast protein structure alignment in three dimensions. *Acta Crystallogr D Biol Crystallogr* 60:2256-2268.
13. Krissinel E, Henrick K (2007) Inference of macromolecular assemblies from crystalline state. *J Mol Biol* 372:774-797.
14. Earley KW, et al. (2006) Gateway-compatible vectors for plant functional genomics and proteomics. *Plant J* 45:616-629.
15. Ashkenazy H, Erez E, Martz E, Pupko T, Ben-Tal N (2010) ConSurf 2010: calculating evolutionary conservation in sequence and structure of proteins and nucleic acids. *Nucleic Acids Res* 38:W529-533.
16. Baker NA, Sept D, Joseph S, Holst MJ, McCammon JA (2001) Electrostatics of nanosystems: application to microtubules and the ribosome. *Proc Natl Acad Sci U S A* 98:10037-10041.
17. Notredame C (2010) Computing multiple sequence/structure alignments with the T-coffee package. *Curr Protoc Bioinformatics* Chapter 3:Unit 3 8 1-25.
18. Gouet P, Robert X, Courcelle E (2003) ESPript/ENDscript: Extracting and rendering sequence and 3D information from atomic structures of proteins. *Nucleic Acids Res* 31:3320-3323.